

Received April 12, 2019, accepted May 4, 2019, date of publication May 16, 2019, date of current version June 3, 2019.

Digital Object Identifier 10.1109/ACCESS.2019.2917331

# Direct Levitation Force Control for a Bearingless Induction Motor Based on Model Prediction

JIANG LU<sup>1</sup>, ZEBIN YANG<sup>1</sup>, XIAODONG SUN<sup>1,2</sup>, (Senior Member, IEEE),  
CHUNFENG BAO<sup>1</sup>, AND XI CHEN<sup>1</sup>

<sup>1</sup>School of Electrical and Information Engineering, Jiangsu University, Zhenjiang 212013, China

<sup>2</sup>Automotive Engineering Research Institute, Jiangsu University, Zhenjiang 212013, China

Corresponding authors: Zebin Yang (zbyang@ujs.edu.cn) and Xiaodong Sun (xdsun@ujs.edu.cn)

This work was supported in part by the National Natural Science Foundation of China under Project 51475214 and Project 51875261, in part by the “333 Project” of Jiangsu Province under Project BRA2017441, in part by the Natural Science Foundation of Jiangsu Province of China under Project BK20180046 and Project BK20170071, in part by the “Qinglan Project” of Jiangsu Province, in part by the Key Project of Natural Science Foundation of Jiangsu Higher Education Institutions under Project 17KJA460005, in part by the Six Categories Talent Peak of Jiangsu Province under Project 2015-XNYQC-003 and Project 2016-GDZB-096, and in part by the Priority Academic Program Development of Jiangsu Higher Education Institutions (PAPD).

**ABSTRACT** Aiming at the high-performance operation requirements of a bearingless induction motor (BIM), a direct levitation force control strategy based on model prediction for the BIM is proposed. Based on mathematical models of the BIM, the flux linkage at the next moment is predicted according to the current observation value of the flux linkage of levitation force winding, and the objective function of the flux linkage is constructed to output the optimal flux linkage. Inverter drive control signals are generated from the SVPWM module to control the BIM levitation. In addition, to deal with the problem of the initial error caused by reverse electromotive force integration in the traditional observation of flux linkage during the process of motor control, an improved flux observer is introduced and applied to the control system. The simulation and experimental results show that the proposed control strategy cannot only effectively improve the suspension stability of the rotor, but also enhance the anti-disturbance ability of the system in comparison to the traditional levitation force control. In the meantime, it has a good dynamic and static performance which verifies the effectiveness and reliability of the proposed control strategy.

**INDEX TERMS** Direct control, bearingless induction motor, model prediction, levitation force, objective function, flux observer.

## I. INTRODUCTION

In recent years, with the progress of technology and the development of industry, higher and higher requirements are applied to the motors' quality and performance. Under this background, the bearingless induction motor (BIM) emerges as the times require [1]–[7]. A BIM combines the traditional induction motor with magnetic bearings, it not only has the advantages of the magnetic bearing, but also has the advantages of no friction, no lubrication, easy maintenance, high reliability, long service life and so on [8]–[11]. It has a broad application in the fields of aerospace, high-speed hard disk, flywheel energy storage, biomedicine and special electric fields of aseptic and no pollution operation. Therefore, the BIM is one of the most valuable motors and have

attracted the attention of many experts and scholars at home and abroad [12]–[17].

With the maturity of the motor control technology, the control technology of the BIM is also constantly improving. The control of the BIM is mainly divided into two parts: torque control and levitation control. In [18], dynamic decoupling between electromagnetic torque and levitation force of the BIM is realized by using alpha-order inverse system method based on least squares support vector machine (LS-SVM). Compared with the traditional vector control, the direct torque control based on space vector pulse width modulation (SVPWM) can effectively solve the problems of large amount of calculation caused by coordinate transformation and the influence of motor parameters on the control performance of the system in the vector control. In addition, it makes the torque ripple smaller, torque response faster and has a good dynamic and static performance [19]–[23]. In the

The associate editor coordinating the review of this manuscript and approving it for publication was Fangfei Li.

levitation control of motor, the radial position of rotor is often controlled by PID regulation, force/current and coordinate transformation. In [24], a method of rotor vibration feedforward compensation control for a BIM Based on coordinate transformation is proposed, which suppresses the vibration of the rotor and improves the suspension performance of the rotor. However, this method converts the compensated radial levitation force into levitation control current, which is an indirect control of levitation force, and has some shortcomings such as slow dynamic response and complicated calculation. In [25], a direct control of rotor radial displacement for a bearingless permanent magnet synchronous motor (PMSM) is proposed, which realizes the stable suspension of the rotor. However, this method is only a single closed-loop indirect control of the rotor radial displacement, and the control precision is not high. In [26], a direct levitation force control method for a bearingless permanent magnet synchronous motor is proposed. The air gap flux of torque winding is obtained by integrating the back EMF of torque winding, and the feedback radial levitation force is calculated to realize the closed-loop control of the system. The method realizes direct control of levitation force, and the system has fast dynamic response and high control accuracy. However, the pure integral part will bring initialization error and cause deviation to flux estimation.

This paper derives the polar coordinate form of the mathematical model of radial levitation force of the BIM, establishes the direct levitation force control system of the BIM by using the traditional direct torque control theory and model predictive control theory [27], [28], and introduces a improved flux observer view to overcome the shortcomings of the back EMF method in flux observation [29]–[34]. Compared with the traditional levitation force control method, this method does not need the closed loop control of levitation current and simplifies the levitation control. The simulation model was built by using MATLAB / Simulink software, and the experiment was carried out on an experimental prototype of the BIM. Simulation and experimental results show that the proposed control method has good dynamic and static performance and is more conducive for online implementation, which verifies the reliability of the method.

## II. MATHEMATICAL MODEL OF THE BIM

There are two sets of windings in the stator of the BIM, their pole number are  $P_1$  and  $P_2$  respectively. The inhomogeneity of the magnetic field in the air gap of the motor is controlled by the interaction of the current in the two sets of windings to produce the controllable radial force acting on the rotor. In order to realize the stable suspension of the bearingless induction motor, the two sets of windings need to meet three conditions [35]:

- 1)  $P_1 = P_2 \pm 1$ ;
- 2) electric angular frequency  $\omega_1 = \omega_2$ ;
- 3) rotating magnetic field in the same direction

The mathematical model of the BIM includes the rotating part and the suspension part.

### A. MATHEMATICAL MODEL OF THE ROTATING PART

The mathematical model of the rotating part of the BIM in the  $\alpha - \beta$  coordinates has the form as:

$$\begin{cases} \frac{di_{1s\alpha}}{dt} = \frac{1}{\sigma L_{1s} T_{1r}} \psi_{1s\alpha} + \frac{1}{\sigma L_{1s}} \omega_r \psi_{1s\beta} - \omega_r i_{1s\beta} \\ \quad + \frac{u_{1s\alpha}}{\sigma L_{1s}} - \frac{R_{1s} L_{1r} + R_{1r} L_{1s}}{\sigma L_{1s} L_{1r}} i_{1s\alpha} \\ \frac{di_{1s\beta}}{dt} = \frac{1}{\sigma L_{1s} T_{1r}} \psi_{1s\beta} - \frac{1}{\sigma L_{1s}} \omega_r \psi_{1s\alpha} + \omega_r i_{1s\alpha} \\ \quad + \frac{u_{1s\beta}}{\sigma L_{1s}} - \frac{R_{1s} L_{1r} + R_{1r} L_{1s}}{\sigma L_{1s} L_{1r}} i_{1s\beta} \\ \frac{d\psi_{1s\alpha}}{dt} = -R_{1s} i_{1s\alpha} + u_{1s\alpha} \\ \frac{d\psi_{1s\beta}}{dt} = -R_{1s} i_{1s\beta} + u_{1s\beta} \end{cases} \quad (1)$$

where  $i_{1s\alpha}$  and  $i_{1s\beta}$  are the stator current of the torque winding in the  $\alpha - \beta$  coordinates respectively;  $L_{1s}$ ,  $L_{1r}$  and  $L_{1m}$  are the stator inductance, the rotor inductance and the mutual inductance of the torque winding respectively;  $\omega_r$  is the rotor speed;  $\psi_{1s\alpha}$  and  $\psi_{1s\beta}$  are the components of the stator flux linkage of the torque winding in the  $\alpha - \beta$  coordinates respectively;  $R_{1s}$  and  $R_{1r}$  are the stator and rotor resistances of the torque winding in the  $\alpha - \beta$  coordinates respectively;  $\sigma = 1 - L_{1m}^2 / (L_{1s} L_{1r})$  is the flux linkage coefficient;  $T_r = L_r / R_r$  is the time constant of rotor. The torque equation of the BIM is given as follows:

$$T_e = P_1(\psi_{1s\alpha} i_{1s\beta} + \psi_{1s\beta} i_{1s\alpha}) \quad (2)$$

### B. MATHEMATICAL MODEL OF THE SUSPENSION PART

The expression of Maxwell force acting on the micro element  $dA$  on the outer surface area of the rotor of the BIM is [34]–[36]:

$$dF = \frac{B^2 dA}{2\mu_0} \quad (3)$$

where  $\mu_0$  is permeability of vacuum.  $dA = rl \cdot d\theta$ ,  $r$  and  $l$  are External diameter of the rotor and effective length of the iron core, and  $\theta$  is space angle.  $B$  is the air gap flux density of the motor. The components of maxwell force in the  $x$ - $y$  coordinates are:

$$\begin{cases} dF_x(\theta) = \frac{rl}{2\mu_0} B^2(\theta) \cos \theta d\theta \\ dF_y(\theta) = \frac{rl}{2\mu_0} B^2(\theta) \sin \theta d\theta \end{cases} \quad (4)$$

Ignoring the effects of rotor slot effect and magnetic saturation [37], [38], the air gap flux density of two sets of windings in the BIM is:

$$B(\theta, t) = B_t(\theta, t) + B_s(\theta, t) \quad (5)$$

where the air gap flux density generated by the torque winding is:

$$B_t(\theta, t) = B_t \cos(P_1 \theta - \omega_1 t - \eta) \quad (6)$$

The air gap flux density generated by the levitation winding is:

$$B_s(\theta, t) = B_s \cos(P_2\theta - \omega_2t - \varphi) \quad (7)$$

The expression of radial levitation force in  $x$  and  $y$  directions can be obtained by substituting equation (5) ~ (7) into equation (4) for integral operation [41], [42]:

$$\begin{cases} F_x = F_2^* \cos(\varphi - \eta) \\ F_y = F_2^* \sin(\varphi - \eta) \end{cases} \quad (8)$$

where the amplitude of radial levitation force is:

$$F_2^* = \frac{\pi r l B_t B_s}{2\mu_0} \quad (9)$$

The air gap flux linkage of the torque winding and the levitation winding in each phase are:

$$\begin{cases} \psi_{tm} = \varphi_t N_t = \frac{2r l B_t}{p_M} N_t \\ \psi_{sm} = \varphi_s N_s = \frac{2r l B_s}{p_B} N_s \end{cases} \quad (10)$$

where  $\varphi_t$  and  $N_t$  are the flux and effective turns of the torque winding respectively,  $\varphi_s$  and  $N_s$  are the flux and effective turns of the levitation winding respectively.

Neglecting the current induced by the levitation winding in the rotor, the amplitude of the synthetic flux in three-phase winding is:

$$\begin{cases} \psi_{1m} = \frac{3}{2} \psi_{tm} \\ \psi_{2s} = \frac{3}{2} \psi_{sm} \end{cases} \quad (11)$$

The amplitude of radial levitation force can be obtained by replacing (10) and (11) into (9):

$$F_2^* = \frac{\pi p_M p_B \psi_{1m} \psi_{2s}}{18\mu_0 r l N_t N_s} = k_r \psi_{1m} \psi_{2s} \quad (12)$$

where  $k_r$  is a constant related to motor parameters.  $\psi_{1m}$  and  $\psi_{2s}$  are the amplitude of air gap flux formed by torque winding and the amplitude of flux formed by the levitation winding respectively.

### III. DIRECT LEVITATION FORCE PREDICTIVE CONTROL

#### A. BASIC PRINCIPLE

The traditional levitation force control of the BIM is realized by vector control. This control mode is greatly influenced by motor parameters and is ultimately controlled by the levitation winding current. It is an indirect control, and the precision control of radial levitation force is not ideal. Therefore, a new direct levitation force control method for the BIM Based on model prediction is proposed in this paper. And its vector control diagram is shown in Fig. 1.

Where the  $\alpha$  axis coincides with the axis of A phase winding, and  $\beta$  axis is 90 degrees ahead of them.  $\psi_{1s}$  is the torque winding flux.  $\psi_r$  is the rotor flux, and its angle with the axis

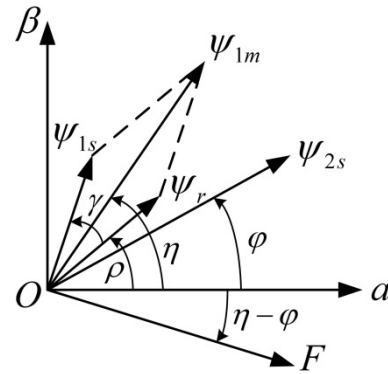


FIGURE 1. Vector diagram of direct levitation force control.

of A phase winding is  $\rho$ .  $\gamma$  is the angle between the torque winding flux and the rotor flux.  $\psi_{1m}$  is the composite air gap flux of the torque winding flux and the rotor flux, and its angle with the axis of A phase winding is  $\eta$ .  $\psi_{2s}$  is the levitation winding flux, and its angle with the axis of A phase winding is  $\varphi$ .  $F$  is the radial levitation force, and its angle with the axis of A phase winding is  $\eta - \varphi$ . Therefore, the components of the mathematical model of the radial levitation force represented by the flux linkage in the  $\alpha - \beta$  coordinates are [41], [42]:

$$\begin{cases} F_\alpha = k_r \psi_{1m} \psi_{2s} \cos(\varphi - \eta) \\ F_\beta = k_r \psi_{1m} \psi_{2s} \sin(\varphi - \eta) \end{cases} \quad (13)$$

Rewrite the upper form into polar coordinates:

$$F = k_r \psi_{1m} \psi_{2s} \angle(\varphi - \eta) \quad (14)$$

From (14), it can be seen that the radial levitation force is a vector whose amplitude is  $k_r \psi_{1m} \psi_{2s}$ . The direction is determined by the difference of the angle between the levitation winding flux  $\psi_{2s}$  and the air gap flux  $\psi_{1m}$  formed by torque winding. Therefore, in order to generate a stable and controllable radial levitation force, it is necessary to control the magnitude and direction of the air gap flux and the levitation flux. When the motor is in stable operation state, the load torque of the motor will remain unchanged, the magnitude and phase of the air gap flux linkage formed by the torque winding and the angle between flux of the torque winding and the flux of the rotor will remain unchanged. At this time the radial levitation force can be controlled by controlling the magnitude and phase of the levitation winding flux. The basic idea of the direct levitation force predictive control for the BIM is as follows: when the magnitude and phase of air gap flux of the torque winding is known, the magnitude and phase of the current levitation winding flux can be calculated, and the difference of the levitation winding flux can be calculated by the predictive feedback value of the flux. In addition, the objective function is used to select switch state corresponding to the optimal state as the output state of the inverter, which realizes the direct levitation force based on model prediction for the BIM.

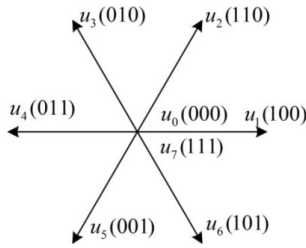


FIGURE 2. Seven voltage vectors of two-level inverter.

**B. IMPLEMENTATION METHOD**

From the above analysis, in order to directly control the levitation force, we must first get the magnitude and phase of the levitation winding flux. At the  $k$  moment, the initial displacement signal is converted by PID control and coordinate transformation in the levitation force control system, and magnitude and phase of the given levitation force are obtained:

$$F(k) = F_g \angle \xi \tag{15}$$

The following formula can be obtained by comparing (14) and (15):

$$\begin{cases} F_g = k_r \psi_{1m} \psi_{2s} \\ \xi = \varphi - \eta \end{cases} \tag{16}$$

The torque winding flux observed by the flux observer is substituted in (16) and the levitation winding flux at the  $k$  moment is obtained by transformation as follows [45], [46]:

$$\begin{cases} \psi_{2s} = F_g / (k_r \psi_{1m}) \\ \varphi = \xi + \eta \end{cases} \tag{17}$$

The components  $\psi_{2s\alpha}^*(k)$  and  $\psi_{2s\beta}^*(k)$  of the levitation winding flux at the  $k$  moment are obtained by transforming (17) into the rectangular coordinates. The predictive values of the flux components of the levitation winding observed by the flux observer at the  $k+1$  moment are  $\psi_{2s\alpha}(k+1)$  and  $\psi_{2s\beta}(k+1)$ . Therefore, the vector difference of the levitation winding flux can be obtained as follows:

$$\begin{cases} \Delta \psi_{2s\alpha} = \psi_{2s\alpha}^*(k+1) - \psi_{2s\alpha}(k) \\ \Delta \psi_{2s\beta} = \psi_{2s\beta}^*(k+1) - \psi_{2s\beta}(k) \end{cases} \tag{18}$$

In the hope of keeping the air gap flux of the torque winding unchanged, the levitation force is controlled by controlling the levitation winding flux. Therefore, the following objective function are constructed:

$$g = ||\psi_{2s}^* - |\psi_{2s}(k+1)|| \tag{19}$$

The BIM is powered by a two-level voltage inverter. As shown in figure 2, there are 8 space voltage vectors, in which  $u_0(000)$  and  $u_7(111)$  are zero vectors [47]. Without restriction, the voltage vectors can be switched arbitrarily at the next moment as shown in figure 3. However, it increases the switching times of the inverter and produces the switching loss and the voltage loss.

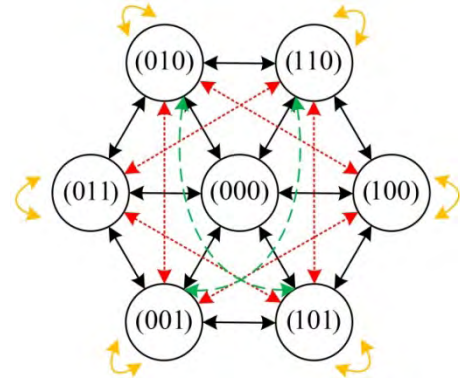


FIGURE 3. Voltage vector switching mode.

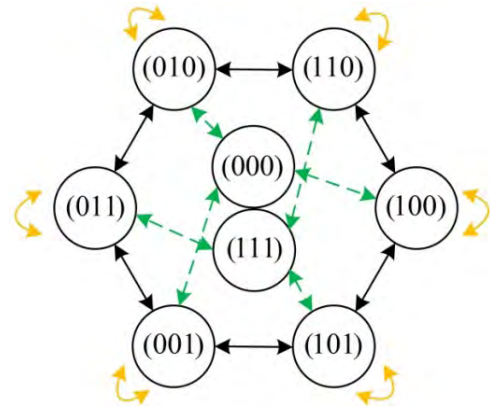


FIGURE 4. Improved voltage vector switching mode.

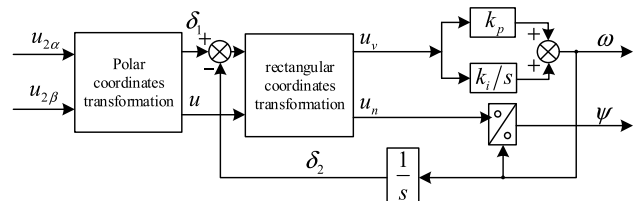


FIGURE 5. Structure diagram of flux observer.

As shown in figure 4, in order to reduce the switching frequency, switching times of switch state should be reduced as much as possible. For example, if the zero vector  $u_0(000)$  and  $u_7(111)$  are fully utilized and when  $u_4(011)$  is switched to zero vector  $u_0(000)$ , it needs to change the inverter switch twice. However, then switch state at the current time can be selected (111) or (010) or (001), this will switch at only one time.

**IV. DESIGN OF A NEW FLUX OBSERVER**

In order to realize the direct levitation force predictive control for the BIM, it is necessary to observe the flux of torque winding and levitation winding accurately. Therefore, an improved flux observer is introduced in this paper. Its structure diagram is shown in Figure 5. Here, we take the observation of levitation winding flux as an example for analysis. It can be seen from figure 5 that the input part of the flux observer is the component of the voltage of the levitation winding in



the  $\alpha - \beta$  coordinates, and the amplitude and phase of the voltage of the levitation winding are obtained after the polar transformation;  $v-n$  coordinate is defined as rotating frame, where the directions of  $v$  axis and  $\psi$  is the same, and  $n$  axis advances  $v$  axis 90 degrees;  $k_p = 1$  and  $k_i = 0.001$  are the proportional integral parameters respectively;  $\delta_1$  is phase of input voltage.

From Figure 5, the relationship between the parameters can be obtained as follows:

$$\begin{cases} |u| = \sqrt{u_{2\alpha}^2 + u_{2\beta}^2} \\ \delta_1 = \arctan(u_{2\beta}/u_{2\alpha}) \end{cases} \quad (20)$$

$$\begin{cases} u_v = |u| \cos(\delta_1 - \delta_2) \\ u_n = |u| \sin(\delta_1 - \delta_2) \end{cases} \quad (21)$$

If the motor is in a stable state after a period of time, the following condition is satisfied:

$$\delta_1 - \delta_2 = 90^\circ \quad (22)$$

At this point, the relation of output value can be satisfied as follows, where  $h(s)$  is the closed loop transfer function of the observer.

$$\begin{cases} \delta_2 = \int_0^t \omega dt \\ \psi = u_n/\omega \\ \omega = \delta_1 \cdot h(s) \end{cases} \quad (23)$$

As can be seen from figure 5, it is difficult to obtain the closed-loop transfer function between the voltage phase angle of the levitation winding and the output phase angle of the levitation flux after the polar transformation by using conventional methods. Therefore, the open-loop transfer function of the system can be obtained first, and then the closed-loop transfer function can be obtained. To solve the transfer function of the system, the following assumptions are made:

(1) a small enough error angle  $\Delta\delta_1$  of levitation winding voltage phase angle is given.

(2) the flux observation system maintains a stable working state, which satisfies (22).

If a small disturbance is input to the system, and the angle error  $\Delta\delta_1$  is caused. Then, the following formula can be get:

$$\begin{aligned} u_v &= |u| \sin(\delta_1 - \delta_2 + \Delta\delta_1) \\ &= |u| \sin \Delta\delta_1 \\ &\approx |u| \Delta\delta_1 \end{aligned} \quad (24)$$

At this time, the relationship between the changing phase angle  $\Delta\delta_2$  of the levitation winding flux and  $\Delta\delta_1$  is as follows:

$$\Delta\delta_2(s) = \frac{u_v}{s} (k_p + \frac{k_i}{s}) = \frac{1}{s} (k_p + \frac{k_i}{s}) \Delta\delta_1(s) \quad (25)$$

The closed loop transfer function of the system can be obtained by (25):

$$y(s) = \frac{\Delta\delta_2(s)}{\Delta\delta_1(s)} = \frac{1}{s} (k_p + \frac{k_i}{s}) \quad (26)$$

Therefore, the error transfer function  $h(s)$  of the system can be obtained as follows:

$$h(s) = \frac{y(s)}{1 + y(s)} = \frac{k_i + k_p s}{s^2 + k_p s + k_i} \quad (27)$$

From this, the components of the levitation winding flux in the  $\alpha - \beta$  coordinates can be calculated as:

$$\begin{cases} \psi_{2s\alpha} = \frac{u_n}{\omega} \cos \delta_2 = \frac{u_n \cos \delta_2}{[\delta_1 \cdot h(s)]} \\ \psi_{2s\beta} = \frac{u_n}{\omega} \sin \delta_2 = \frac{u_n \sin \delta_2}{[\delta_1 \cdot h(s)]} \end{cases} \quad (28)$$

Similarly, the components of the torque winding flux in the  $\alpha - \beta$  coordinates can be obtained. The expression is similar to (28). The amplitude and phase of the torque winding flux are:

$$\begin{cases} \psi_{1s} = \sqrt{\psi_{1s\alpha}^2 + \psi_{1s\beta}^2} \\ \mu = \arctan(\psi_{1s\beta}/\psi_{1s\alpha}) \end{cases} \quad (29)$$

It is assumed that the rotor flux is  $\psi_r$  and the stator leakage inductance of the torque winding is  $L_{1l}$ , then the expression of the synthetic air gap flux between the torque winding flux and the rotor flux in the  $\alpha - \beta$  coordinates is as follows:

$$\begin{cases} \psi_{1m\alpha} = \psi_r \cos \rho + \psi_{1s\alpha} - L_{1l} i_{1s\alpha} \\ \psi_{1m\beta} = \psi_r \sin \rho + \psi_{1s\beta} - L_{1l} i_{1s\beta} \end{cases} \quad (30)$$

The amplitude and phase of the synthetic air gap flux of the torque winding can be obtained:

$$\begin{cases} \psi_{1m} = \sqrt{\psi_{1m\alpha}^2 + \psi_{1m\beta}^2} \\ \eta = \arctan(\psi_{1m\beta}/\psi_{1m\alpha}) \end{cases} \quad (31)$$

Plug the component of the levitation winding flux in the  $\alpha - \beta$  coordinates obtained by the flux observer and the amplitude and phase of the synthetic air gap flux of the torque winding into the levitation control system, then the levitation force is directly controlled by a series of transformations.

Since the phase difference reflects the performance of the loop, it is assumed that frequency of the input signal is:

$$\omega'_i = \alpha \omega_i \quad (32)$$

Then the change of the input phase with time is:

$$\delta_1(t) = \int_0^t \omega'_i(\tau) d\tau = \alpha t \quad (33)$$

Formula(34)can be obtained by Laplace transform:

$$\delta_1(s) = \alpha/s^2 \quad (34)$$

The stable phase error is obtained by final value theorem:

$$\Delta\delta(\infty) = \lim_{t \rightarrow \infty} \Delta\delta(t) = \lim_{s \rightarrow 0} s \cdot \delta_1(s) \cdot h(s) = 0 \quad (35)$$

Form (35),we can know that when the input signal has error, the phase difference can still maintain a certain value. This shows that the flux observer proposed in this paper has good tracking performance and robustness.

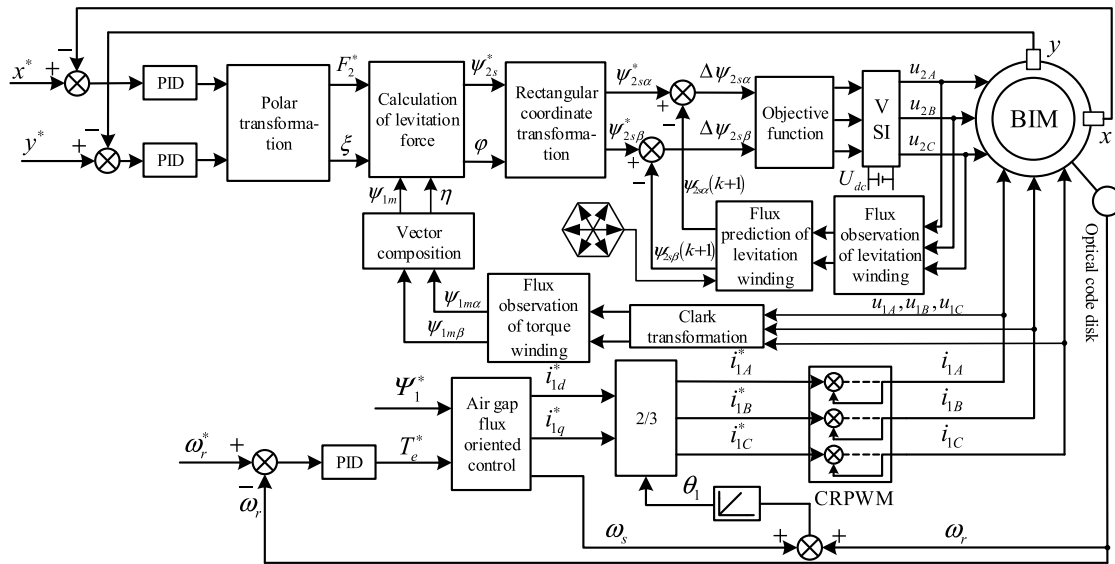


FIGURE 6. The block diagram of the direct levitation force control based on model prediction for the BIM.

TABLE 1. Parameters of the BIM.

Parameters(unit)	Torque winding	Levitation winding
Rated power (kW)	1	0.5
Rated current (A)	2.86	2.86
Stator resistance (Ω)	2.01	1.03
Rotor resistance (Ω)	11.48	0.075
Mutual inductance of stator and rotor (mH)	158.56	9.32
Stator leakage inductance (mH)	4.45	2.67
Rotor leakage inductance (mH)	9.22	5.42
Rotational inertia (kg·m <sup>2</sup> )	0.00769	0.00769
Rotor mass (kg)	2.85	2.85
Stator inner diameter (mm)	98	98
Core length (mm)	105	105
Pole pairs	1	2

V. SYSTEM SIMULATION AND EXPERIMENTAL RESULTS ANALYSIS

A. SYSTEM SIMULATION PARAMETERS AND CONTROL BLOCK DIAGRAM

To verify the feasibility of the proposed control strategy, the Simulink toolbox in Matlab is employed to build the system model of the traditional levitation force control and direct levitation force control for the BIM. The parameters of the BIM used in the simulation are listed in Table 1.

The block diagram of the direct levitation force control based on model prediction for the BIM is shown in Figure 6. It can be seen from the figure that the components of levitation force is obtained according to the difference between the displacement signal  $x$  and  $y$  measured by the displacement

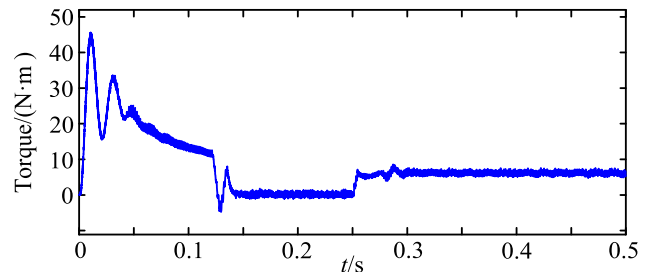


FIGURE 7. Torque characteristic curve.

sensor and the given displacement signal  $x^*$  and  $y^*$  which are adjusted by PID. The amplitude and phase of the radial levitation force are obtained by polar transformation, and then the amplitude  $\psi_{2s}^*$  and phase  $\xi$  of the levitation winding flux is calculated by the air gap flux of the torque winding observed by the torque winding flux observer. The reference values  $\psi_{2s\alpha}^*$  and  $\psi_{2s\beta}^*$  of the levitation winding flux are obtained by rectangular coordinate transformation. The difference between the reference values  $\psi_{2s\alpha}^*$  and  $\psi_{2s\beta}^*$  of the levitation winding flux and the predicted flux  $\psi_{2s\alpha}(k + 1)$  and  $\psi_{2s\beta}(k + 1)$  at the next moment is calculated. In addition, The flux under optimal switch state is selected by the objective function and modulated by SVPWM to produce voltage signal to drive the inverter. Finally, the three-phase voltage needed to control the motor is obtained, and the direct levitation force control based on model prediction for the BIM is realized.

B. SIMULATION RESULTS AND ANALYSIS

Figures 7 and 8 are the torque and speed characteristic curves of the BIM when the control method adopted in this paper is used. As can be seen from Figure 4, the torque of the motor reaches the maximum value when starting, then decreases and reaches the stable value quickly. When the load is suddenly

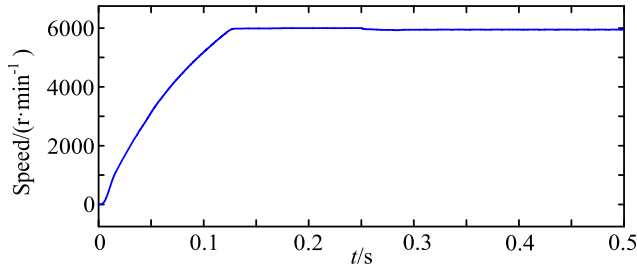


FIGURE 8. Speed characteristic curve.

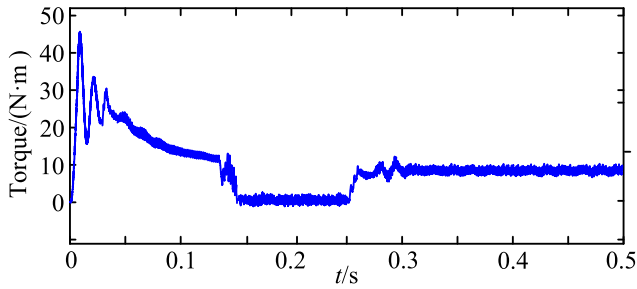


FIGURE 9. Torque characteristic curve.

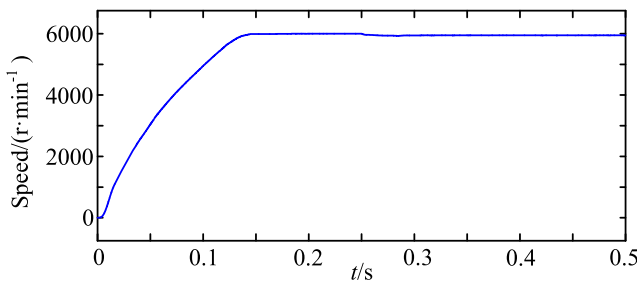
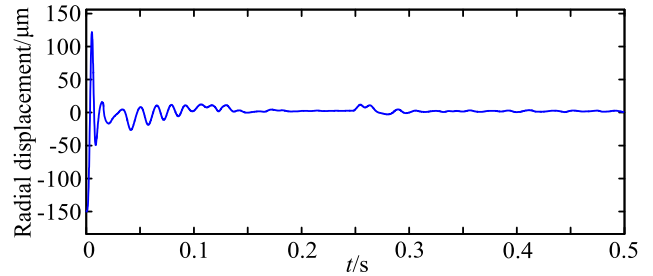


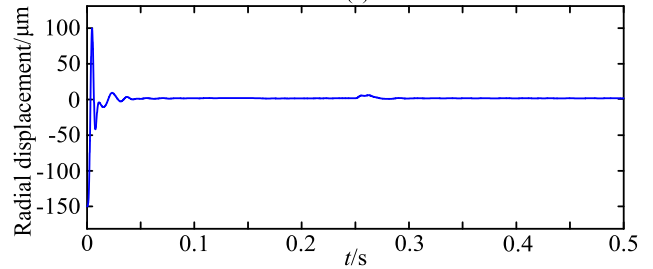
FIGURE 10. Speed characteristic curve.

added at 0.25s, the torque increases but tends to be stable quickly. When the torque is stable, the torque fluctuation is small. Fig. 5 shows that the motor achieves a given speed of 6000r/min at 0.125s, and the speed response is faster. When the motor is suddenly loaded at 0.25s, the speed decreases slightly, but the change is not obvious and can reach a stable state quickly. Figures 9 and 10 are the torque and speed characteristic curves of the BIM when the traditional levitation force control is adopted. From the figures, it can be seen that the torque response and speed response of the traditional levitation force control are slower than that of the direct levitation force control, and can not achieve good control effect.

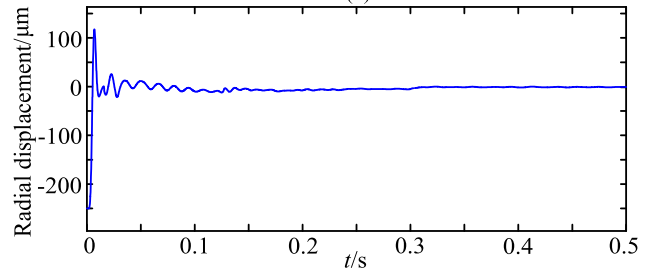
Figure 11 shows the radial displacement waveforms of the rotor when the two kinds of levitation force control methods are adopted. Figure 11(a) and 11(b) are the displacement waveforms of the rotor in  $x$  and  $y$  directions when the conventional levitation force vector control method is used. Figure 11(c) and 11(d) are the displacement waveforms in  $x$  and  $y$  directions when the direct levitation force control method based on model prediction proposed in this paper is used. Compared with the two methods, it can be seen that the rotor can realize stable suspension more quickly and the suspension fluctuation is less. When the load is suddenly



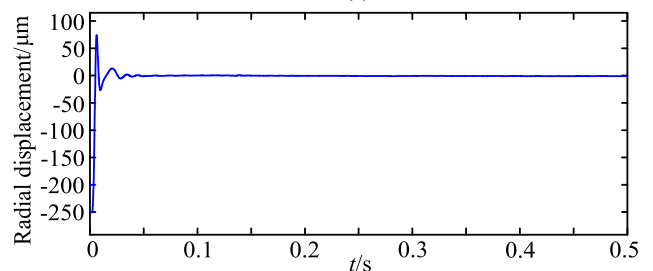
(a)



(b)



(c)



(d)

FIGURE 11. Radial displacement waveforms of the rotor. (a) Radial displacement of  $x$  axis. (b) Radial displacement of  $x$  axis. (c) Radial displacement of  $y$  axis. (d) Radial displacement of  $y$  axis.

added at 0.25s, it can be seen from the diagram that the radial displacement fluctuation amplitude of the rotor is smaller, and the system has good dynamic performance and anti-disturbance ability.

Figure 12 shows the trajectory of the rotor in  $x$  and  $y$  directions when the two levitation force control methods are adopted. It can be seen from the figure that, compared with the traditional control method, the motion trajectory of the rotor is reduced and the rotor can enter the stable suspended state more smoothly after adopting the control method proposed in this paper. In conclusion, the proposed control method can effectively improve the suspension performance of the rotor.





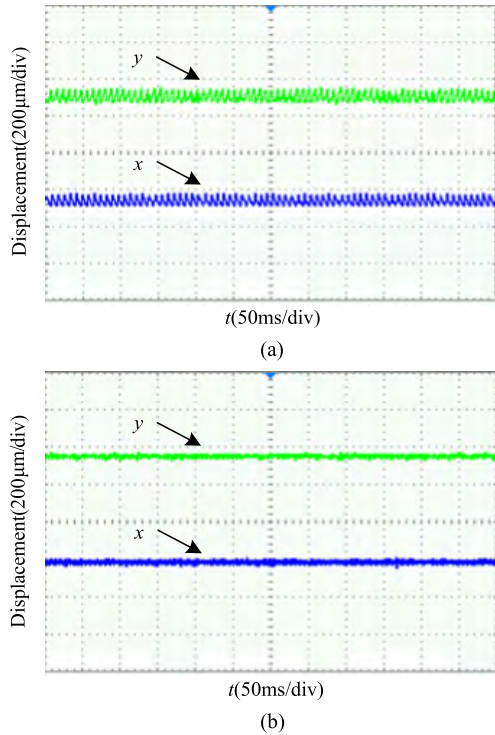


**FIGURE 16.** Experimental diagram of rotor displacement. (a) Traditional levitation force control. (b) Direct levitation force predictive control.

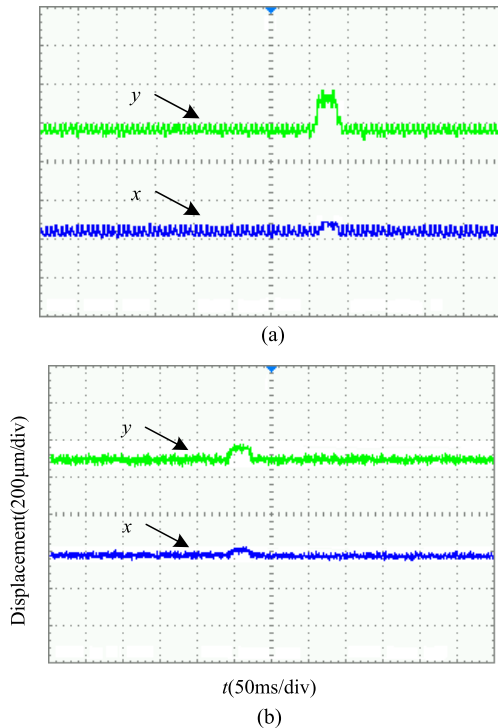


**FIGURE 17.** Experimental diagrams of the rotor subjected to radial disturbance. (a) Traditional levitation force control. (b) Direct levitation force predictive control.

the radial displacement peak value of the rotor in  $x$  and  $y$  directions is  $80\mu\text{ m}$  when the traditional levitation force vector control method is adopted. As can be seen from

figure 16(b), the radial displacement peak value of the rotor in  $x$  and  $y$  directions is  $40\mu\text{ m}$ . Compared with the two methods, the direct levitation force predictive control proposed in this paper can reduce the radial displacement of the rotor, decrease the vibration significantly, and make the suspension more stable.

Figure 17 shows the radial displacement experimental diagram of the rotor in  $x$  and  $y$  directions after adding the same disturbance to the rotor with two control methods. Compared with figure 17(a) and figure 17(b), it can be seen that the radial displacement of the rotor in the  $x$  direction has no obvious change, but the radial displacement in the  $y$  direction changes significantly. The radial displacement of the rotor in the  $y$  direction after disturbance is  $160\mu\text{ m}$  when the traditional levitation force vector control is used, and the radial displacement of the rotor in the  $y$  direction after disturbance is  $100\mu\text{ m}$  when the direct levitation force predictive control is used. In conclusion, the displacement amplitude decreases obviously when the proposed control method is used after the rotor is disturbed, and the control system has better anti-disturbance performance.

## VI. CONCLUSIONS

Referring to the theory of direct torque control, this paper applies it to the levitation system of the BIM and puts forward a direct levitation force predictive control method which is different from other levitation control methods. Besides, this paper introduces an improved flux observer to observe the flux of the torque winding and the levitation force winding, so as to improve the precision of levitation force control. The simulation and experimental results all show that the direct levitation force control based on model prediction improves the stability of the rotor suspension, reduces the radial displacement fluctuation, enhances the anti-disturbance ability of the suspension system, has good dynamic and static performance, and promotes the further development of the BIM in the field of levitation control.

## REFERENCES

- [1] V. F. Victor, F. O. Quintaes, J. S. B. Lopes, L. D. S. Junior, A. S. Lock, and A. O. Salazar, "Analysis and study of a bearingless AC motor type divided winding, based on a conventional squirrel cage induction motor," *IEEE Trans. Magn.*, vol. 48, no. 11, pp. 3571–3574, Nov. 2012.
- [2] Z. Yang, D. Zhang, X. Sun, and X. Ye, "Adaptive exponential sliding mode control for a bearingless induction motor based on a disturbance observer," *IEEE Access*, vol. 6, pp. 35425–35434, 2018.
- [3] X. Sun, L. Chen, Z. Yang, and H. Zhu, "Speed-sensorless vector control of a bearingless induction motor with artificial neural network inverse speed observer," *IEEE/ASME Trans. Mechatronics*, vol. 18, no. 4, pp. 1357–1366, Aug. 2013.
- [4] Z. Yang, D. Zhang, X. Sun, W. Sun, and L. Chen, "Nonsingular fast terminal sliding mode control for a bearingless induction motor," *IEEE Access*, vol. 5, pp. 16656–16664, 2017.
- [5] W. Bu, X. Zhang, and F. He, "Sliding mode variable structure control strategy of bearingless induction motor based on inverse system decoupling," *IEEE J. Trans. Electr. Electron. Eng.*, vol. 13, pp. 1052–1059, Jul. 2018.
- [6] X. Sun et al., "Performance analysis of suspension force and torque in an IBPMSM with V-shaped PMs for flywheel batteries," *IEEE Trans. Magn.*, vol. 54, no. 11, Nov. 2018, Art. no. 8105504.

- [7] A. Chiba and J. A. Santisteban, "A PWM harmonics elimination method in simultaneous estimation of magnetic field and displacements in bearingless induction motors," *IEEE Trans. Ind. Appl.*, vol. 48, no. 1, pp. 124–131, Jan./Feb. 2012.
- [8] X. Sun, B. Su, L. Chen, Z. Yang, X. Xu, and Z. Shi, "Precise control of a four degree-of-freedom permanent magnet biased active magnetic bearing system in a magnetically suspended direct-driven spindle using neural network inverse scheme," *Mech. Syst. Signal Process.*, vol. 88, pp. 36–48, May 2017.
- [9] X. Sun, L. Chen, H. Jiang, Z. Yang, J. Chen, and W. Zhang, "High-performance control for a bearingless permanent-magnet synchronous motor using neural network inverse scheme plus internal model controllers," *IEEE Trans. Ind. Electron.*, vol. 63, no. 6, pp. 3479–3488, Jun. 2016.
- [10] A. O. Salazar and R. M. Stephan, "A bearingless method for induction machines," *IEEE Trans. Magn.*, vol. 29, no. 6, pp. 2965–2967, Nov. 1993.
- [11] X. Sun, B. Su, L. Chen, Z. Yang, J. Chen, and W. Zhang, "Nonlinear flux linkage modeling of a bearingless permanent magnet synchronous motor based on AW-LSSVM regression algorithm," *Int. J. Appl. Electromagn. Mech.*, vol. 51, pp. 151–159, Jun. 2016.
- [12] A. Chiba and J. Asama, "Influence of rotor skew in induction type bearingless motor," *IEEE Trans. Magn.*, vol. 48, no. 11, pp. 4646–4649, Nov. 2012.
- [13] X. Sun, Y. Shen, S. Wang, G. Lei, Z. Yang, and S. Han, "Core losses analysis of a novel 16/10 segmented rotor switched reluctance BSG motor for HEVs using nonlinear lumped parameter equivalent circuit model," *IEEE/ASME Trans. Mechatronics*, vol. 23, no. 2, pp. 747–757, Apr. 2018.
- [14] Y.-K. He, H. Nian, and B.-T. Ruan, "Optimized air-gap-flux orientated control of an induction-type bearingless motor," *Proc. Chin. Soc. Elect. Eng.*, vol. 24, no. 6, pp. 116–121, Jun. 2004.
- [15] A. Sinervo and A. Arkkio, "Rotor radial position control and its effect on the total efficiency of a bearingless induction motor with a cage rotor," *IEEE Trans. Magn.*, vol. 50, no. 4, pp. 1–9, Apr. 2014.
- [16] X. Sun, L. Chen, and Z. Yang, "Overview of bearingless permanent-magnet synchronous motors," *IEEE Trans. Ind. Electron.*, vol. 60, no. 12, pp. 5528–5538, Dec. 2013.
- [17] W. S. Bu, C. Zu, S. Wang, and S. Huang, "Digital control system design and analyses of a 3-phase bearingless induction motor," *Turkish J. Elect. Eng. Comput. Sci.*, vol. 22, no. 5, pp. 1193–1209, Jan. 2014.
- [18] Z. Q. Wang and X. L. Huang, "Nonlinear decoupling control for bearingless induction motor based on support vector machines inversion," *Trans. Chin. Electro. Soc.*, vol. 30, no. 10, pp. 164–170, May 2015.
- [19] Z. Shi et al., "Torque analysis and dynamic performance improvement of a PMSM for EVs by skew angle optimization," *IEEE Trans. Appl. Supercond.*, vol. 29, no. 2, Mar. 2019, Art. no. 0600305.
- [20] M. Bermudez, I. Gonzalez-Prieto, F. Barrero, H. Guzman, M. J. Duran, and X. Kestelyn, "Open-phase fault-tolerant direct torque control technique for five-phase induction motor drives," *IEEE Trans. Ind. Electron.*, vol. 64, no. 2, pp. 902–911, Feb. 2017.
- [21] X. G. Lin, Y. Z. Zhou, and M. Cheng, "A novel direct torque control for six-phase permanent magnet synchronous motor with two opened phases based on defining fictitious variables," *Proc. Chin. Soc. Elect. Eng.*, vol. 36, no. 1, pp. 231–239, Jan. 2016.
- [22] X. D. Sun, Z. Shi, Z. B. Yang, S. H. Wang, B. K. Su, L. Chen, and K. Li, "Digital control system design for bearingless permanent magnet synchronous motors," *Bull. Pol. Acad. Sci.-Tech. Sci.*, vol. 66, no. 5, pp. 687–698, Oct. 2018.
- [23] X. Sun et al., "Performance improvement of torque and suspension force for a novel five-phase BFSPM machine for flywheel energy storage systems," *IEEE Trans. Appl. Supercond.*, vol. 29, no. 2, Mar. 2019, Art. no. 0601505.
- [24] Z. Yang, D. Dong, H. Gao, X. Sun, R. Fan, and H. Zhu, "Rotor mass eccentricity vibration compensation control in bearingless induction motor," *Adv. Mech. Eng.*, vol. 7, no. 1, Jan. 2015, Art. no. 168428.
- [25] S. Zhang and F. L. Luo, "Direct control of radial displacement for bearingless permanent-magnet-type synchronous motors," *IEEE Trans. Ind. Electron.*, vol. 56, no. 2, pp. 542–552, Feb. 2009.
- [26] T. Zhang, X. Sun, W. Pan, and H. Zhu, "Direct suspension force control of bearingless permanent magnet synchronous motor," in *Proc. IEEE CCDC*, Taiyuan, China, May 2012, pp. 3004–3008.
- [27] F. Y. Chen, W. Hua, W. T. Huang, J. G. Zhu, and M. H. Tong, "Open-circuit fault-tolerant strategies for a five-phase flux-switching permanent magnet motor based on model predictive torque control method," *Proc. Chin. Soc. Elect. Eng.*, vol. 39, no. 2, pp. 337–346, Jan. 2019.
- [28] Y. Luo and C. Liu, "A flux constrained predictive control for a six-phase PMSM motor with lower complexity," *IEEE Trans. Ind. Electron.*, vol. 66, no. 7, pp. 5081–5093, Jul. 2019.
- [29] H. M. Basri and S. Mekhilef, "Experimental evaluation of model predictive current control for a modified three-level four-leg indirect matrix converter," *IET Electr. Power Appl.*, vol. 12, no. 1, pp. 114–123, Jan. 2018.
- [30] Y. Zhou, D. Li, J. Lu, Y. Xi, and L. Cen, "Networked and distributed predictive control of non-linear systems subject to asynchronous communication," *IET Control Theory Appl.*, vol. 12, no. 4, pp. 504–514, Mar. 2018.
- [31] M. R. Nasiri, S. Farhangi, and J. Rodríguez, "Model predictive control of a multilevel CHB STATCOM in wind farm application using diophantine equations," *IEEE Trans. Ind. Electron.*, vol. 66, no. 2, pp. 1213–1223, Feb. 2019.
- [32] L. M. A. Caseiro, A. M. S. Mendes, and S. M. A. Cruz, "Dynamically weighted optimal switching vector model predictive control of power converters," *IEEE Trans. Ind. Electron.*, vol. 66, no. 2, pp. 1235–1245, Feb. 2019.
- [33] U. Rosolia and F. Borrelli, "Learning model predictive control for iterative tasks. A data-driven control framework," *IEEE Trans. Autom. Control*, vol. 63, no. 7, pp. 1883–1896, Jul. 2018.
- [34] H. Heydari-Doostabad and R. Ghazi, "A new approach to design an observer for load current of UPS based on Fourier series theory in model predictive control system," *Int. J. Elect. Power Energy Syst.*, vol. 104, pp. 898–909, Jan. 2019.
- [35] T. Matsuzaki, M. Takemoto, S. Ogasawara, S. Ota, K. Oi, and D. Matsushashi, "Operational characteristics of an IPM-type bearingless motor with 2-pole motor windings and 4-pole suspension windings," *IEEE Trans. Ind. Appl.*, vol. 53, no. 6, pp. 5383–5392, Nov. 2017.
- [36] X. Sun et al., "Suspension force modeling for a bearingless permanent magnet synchronous motor using Maxwell stress tensor method," *IEEE Trans. Appl. Supercond.*, vol. 26, no. 7, Oct. 2016, Art. no. 0608705.
- [37] A. Bermúdez, A. L. Rodríguez, and I. Villar, "Extended formulas to compute resultant and contact electromagnetic force and torque from maxwell stress tensors," *IEEE Trans. Magn.*, vol. 53, no. 4, Apr. 2017, Art. no. 7200409.
- [38] F. Rezaee-Alam, B. Rezaeealam, and J. Faiz, "Unbalanced magnetic force analysis in eccentric surface permanent-magnet motors using an improved conformal mapping method," *IEEE Trans. Energy Convers.*, vol. 32, no. 1, pp. 146–154, Mar. 2017.
- [39] L. Chang and T. M. Jahns, "Prediction and evaluation of PWM-induced current ripple in IPM machines incorporating slotting, saturation, and cross-coupling effects," *IEEE Trans. Ind. Appl.*, vol. 54, no. 6, pp. 6015–6026, Nov. 2018.
- [40] H. H. Mortensen, F. Innings, and A. Håkansson, "Local levels of dissipation rate of turbulent kinetic energy in a rotor–stator mixer with different stator slot widths—An experimental investigation," *Chem. Eng. Res. Des.*, vol. 130, pp. 52–62, Feb. 2018.
- [41] W. Chen, Y. Xu, Z. Wang, L. Ren, J. Shi, and Y. Tang, "Levitation force computation of HTS/PM system based on  $H$ -formulation," *IEEE Trans. Magn.*, vol. 54, no. 11, Nov. 2018, Art. no. 7402805.
- [42] T. Espenhahn, D. Berger, L. Schultz, K. Nielsch, and R. Hühne, "Simulation of force generation above magnetic tracks for superconducting levitation systems," *IEEE Trans. Appl. Supercond.*, vol. 28, no. 4, Jun. 2018, Art. no. 3600205.
- [43] E. Severson, R. Nilssen, T. Undeland, and N. Mohan, "Design of dual purpose no voltage combined windings for bearingless motors," *IEEE Trans. Ind. Appl.*, vol. 53, no. 5, pp. 4368–4379, Sep./Oct. 2017.
- [44] X. Sun, Z. Shi, L. Chen, and Z. Yang, "Internal model control for a bearingless permanent magnet synchronous motor based on inverse system method," *IEEE Trans. Energy Convers.*, vol. 31, no. 4, pp. 1539–1548, Dec. 2016.
- [45] L. Zampieri, J. C. Miller, and R. Turolla, "Time-dependent analysis of spherical accretion on to black holes," *Monthly Notices Roy. Astronomical Soc.*, vol. 281, no. 4, pp. 1183–1196, Aug. 2018.
- [46] M. Yang, X. Lang, J. Long, and D. Xu, "Flux immunity robust predictive current control with incremental model and extended state observer for PMSM drive," *IEEE Trans. Power Electron.*, vol. 32, no. 12, pp. 9267–9279, Dec. 2017.
- [47] A. Shafiei, B. M. Dehkordi, A. Kiyomars, and S. Farhangi, "A control approach for a small-scale PMSG-based WECS in the whole wind speed range," *IEEE Trans. Power Electron.*, vol. 32, no. 12, pp. 9117–9130, Dec. 2017.



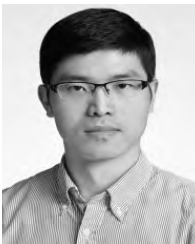
**JIANG LU** was born in Taizhou, Jiangsu, China, in 1993. He is currently pursuing the master's degree with Jiangsu University. His main research interest includes bearingless induction motor and its intelligent control.



**CHUNFENG BAO** was born in Nantong, Jiangsu, China, in 1993. He is currently pursuing the master's degree with Jiangsu University. His main research interest includes the structural optimization design of the bearingless motor.



**ZEBIN YANG** received the B.Sc., M.Sc., and Ph.D. degrees in electrical engineering from Jiangsu University, Zhenjiang, China, in 1999, 2004, and 2013, respectively, where he is currently a Professor. From 2014 to 2015, he was a Visiting Scholar with the School of Electrical, Mechanical, and Mechatronic Systems, University of Technology Sydney, Sydney, NSW, Australia. His main research interests include drives and control for bearingless motors, and magnetic levitation transmission technology.



**XIAODONG SUN** (M'12–SM'18) received the B.Sc. degree in electrical engineering and the M.Sc. and Ph.D. degrees in control engineering from Jiangsu University, Zhenjiang, China, in 2004, 2008, and 2011, respectively.

Since 2004, he has been with Jiangsu University, where he is currently a Professor with the Automotive Engineering Research Institute. From 2014 to 2015, he was a Visiting Professor with the School of Electrical, Mechanical, and Mechatronic Systems, University of Technology Sydney, Sydney, NSW, Australia. His current teaching and research interests include electrical machines and drives, drives and control for electric vehicles, and intelligent control. He has authored or coauthored more than 80 refereed technical papers and one book, and holds 36 patents in his areas of interest.



**XI CHEN** was born in Nantong, Jiangsu, China, in 1994. He is currently pursuing the master's degree with Jiangsu University. His main research interest includes bearingless induction motor and its intelligent control.

...